Title
HIGH RESOLUTION COMPUTED TOMOGRAPHY OF POSITRON EMITTERS

Author
Derenzo, S.E.

Publication Date
1976-10-01

Presented at the 1976 Nuclear Science Symposium and Scintillation and Semiconductor Counter Symposium, New Orleans, LA, October 20 - 22, 1976

LBL-4797
c. 1

HIGH RESOLUTION COMPUTED TOMOGRAPHY OF POSITRON EMITTERS

S. E. Derenzo, T. F. Budinger, J. L. Cahoon, R. H. Huesman, and H. G. Jackson

DONNER LABORATORY

October 1976

Prepared for the U. S. Energy Research and Development Administration under Contract W-7405-ENG-48

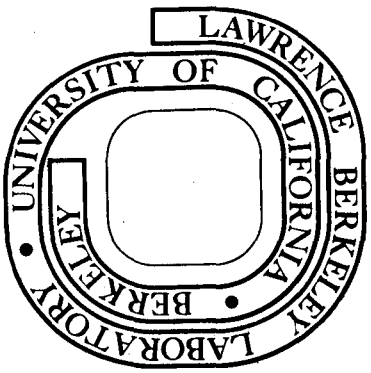

LBL-4797
c. 1

DISCLAIMER

HIGH RESOLUTION COMPUTED TOMOGRAPHY OF POSITRON EMITTERS

S.E. Derenzo, T.F. Budinger, J.L. Cahoon,
R.H. Huesman, and H.G. Jackson,

Donner Laboratory
University of California, Berkeley, California

ABSTRACT

High resolution computed transaxial tomography has been performed on phantoms containing positron-emitting isotopes. The imaging system consisted of two opposing groups of eight NaI(Tl) crystals 8 mm x 30 mm x 50 mm deep and the phantoms were rotated to measure coincident events along 8960 projection integrals as they would be measured by a 280 crystal ring system now under construction. The spatial resolution in the reconstructed images is 7.5 mm FWHM at the center of the ring and approximately 11 mm FWHM at a radius of 10 cm. We present measurements of imaging and background rates under various operating conditions. Based on these measurements, the full 280 crystal system will image 10,000 events per sec with 400 μCi in a section 1 cm thick and 20 cm in diameter. We show that 1.5 million events are sufficient to reliably image 3.5 mm hot spots with 14 mm center-to-center spacing and isolated 9 mm diameter cold spots in phantoms 15-20 cm in diameter.

1. Introduction

The combination of radionuclide techniques and computed tomography has the unique ability to quantitate the amount of an isotope in well-defined regions of the body and thereby deduce the functional or metabolic activity in vivo without discomfort to the patient. During the past 15 years radionuclide computed tomography has been investigated using single photon emitters and positron emitters with a variety of instruments.[1-28]

We have previously described the anticipated properties of a high-resolution 280 crystal positron ring system for computed tomography[17] and compared its properties as measured with the 16 crystal system to single gamma computed tomography from multiple views using an Anger scintillation camera.[28]

In this paper we describe the anticipated properties of a circular ring of 280 rectangular NaI(Tl) crystals for positron computed tomography as simulated by two opposing groups of eight crystals.

In Section 2 we describe:
(1) The physical organization for coupling 8 mm crystals to 38 mm phototubes.
(2) The crystal efficiency and resolution in space, time and energy.
(3) The electronics for simultaneously determining pulse height and position for 15,680 crystal pair combinations spanning a 50 cm field of view.

In Section 3 we report:
(1) The coincidence rates and background fractions under various pulse height and shielding conditions.
(2) The effect of lead and indium scatter filters.
(3) The point and line spread functions in transverse section images.
(4) The ability of the system to image hot and cold spot phantoms.
(5) The estimation of statistical noise in emission computed tomography.

2. System Description

2.1 Physical Organization

The annihilation gamma ray detector consists of a ring of closely packed 8 mm x 30 mm x 50 mm deep NaI(Tl) crystals. In order to couple these crystals to readily available 38 mm phototubes we designed a special set of quartz lightpipes that directs the scintillation light from each crystal into one of five directions (-90°, -60°, 0°, 60°, 90°) and provides sufficient separation for mounting the phototubes.

Figure 1 shows a crystal-lightpipe-phototube assembly and Figure 2 shows five such assemblies mounted in one of the 56 frames that will comprise the full 280 crystal ring.

2.2 Crystals

Rectangular NaI(Tl) crystals were chosen over cylindrical crystals to maximize the detection solid angle. The crystals measure 8 mm x 30 mm x 50 mm deep; the 8 mm dimension was chosen to provide sufficient resolution, for example, to distinguish epi- from endocardium; the 30 mm dimension was chosen to permit sections as thick as 15 mm to be imaged; and the 50 mm depth was chosen to provide detection efficiency without excessive scattering and multiple detections in the crystals. Prototype crystals were supplied by Harshaw Chemical Co. (Solon, Ohio) and Bicron Corp. (Newbury, Ohio). At 511 keV the individual crystals have a photopeak detection efficiency of 25% and for pulses > 100 keV the detection efficiency is 60%. (In this study the efficiencies were lower because about 20% of the detections involved ≥ 2 neighboring crystals and were rejected.) The photopeak resolution is typically 9% FWHM when coupled directly to a bialkali phototube.

The spatial resolution for a pair of crystals 80 cm apart was determined by measuring the coincidence rate as a function of position for 1.2 mm diameter line sources of ^{22}Na, ^{68}Ge and ^{82}Sr. The results (Table I) show that posi-

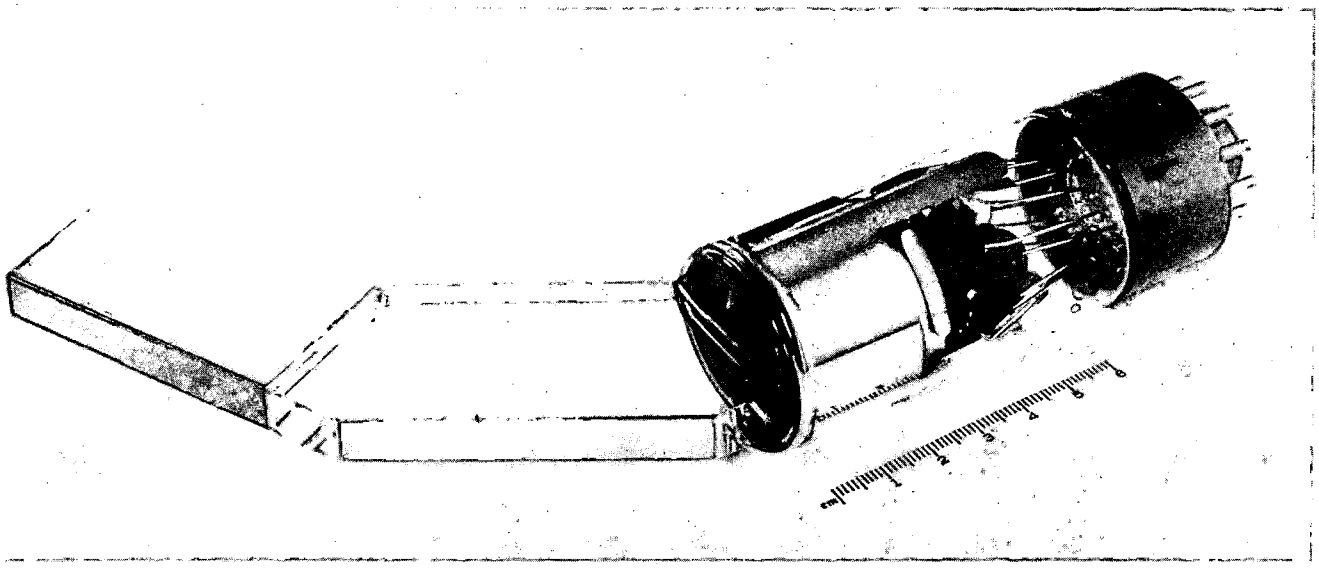

FIG 1: (above) Rectangular NaI(Tl) crystal 8 mm x 30 mm x 50 mm deep mounted in a 9.8 mm wide stainless steel housing and coupled to a 38 mm diameter phototube via a quartz lightpipe. Narrow surface of lightpipe facing bottom of picture is aluminized.

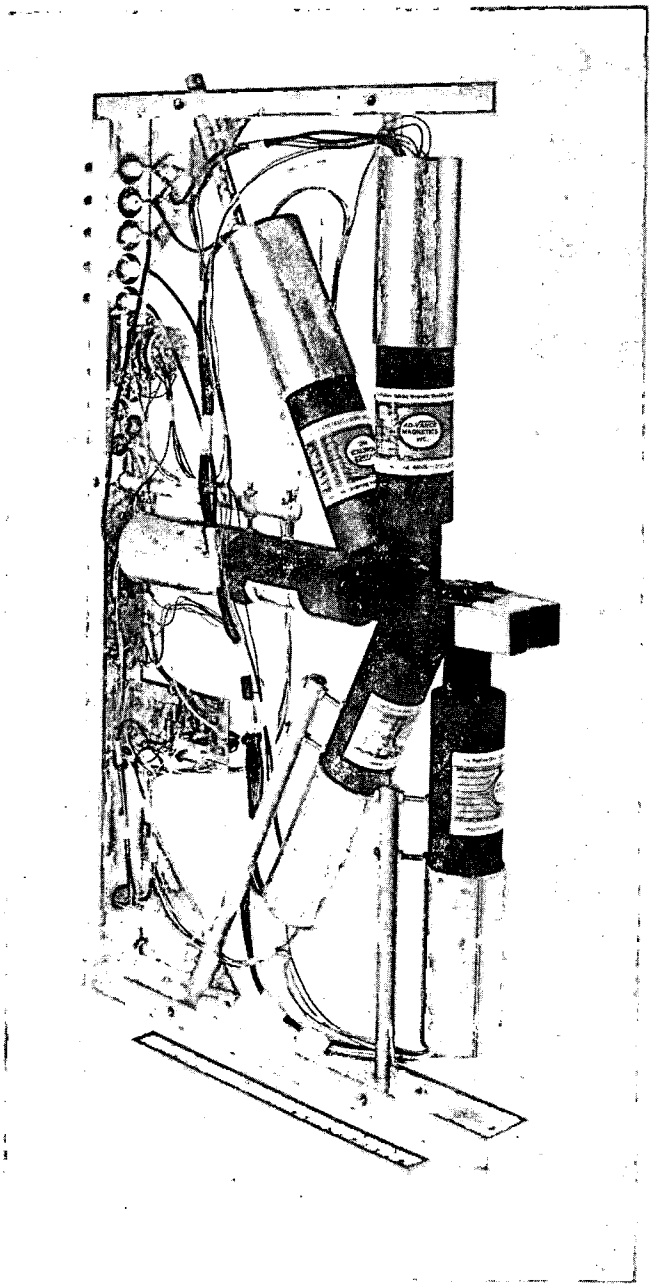

FIG 2: (left) Set of five crystals, lightpipes, phototubes and bases mounted in an aluminum frame. The full 280 crystal system will consist of 56 of these frames.

Table I - Crystal Pair Resolution[a]

Isotope	Maximum Positron Energy (keV)	Source Medium	FWHM(mm)	FW0.1M(mm)
^{22}Na	544	1.3 cm Lucite[b]	5.0 ± 0.2	9.2 ± 0.3
^{22}Na	544	20 cm water	5.0 ± 0.3	9.5 ± 0.4
^{68}Ge	1900	1.3 cm Lucite[b]	6.0 ± 0.2	11.5 ± 0.3
^{68}Ge	1900	20 cm water	6.4 ± 0.3	11.8 ± 0.4
^{82}Sr	3150	1.3 cm Lucite[b]	7.1 ± 0.2	16.5 ± 0.5
^{82}Sr	3150	20 cm water	7.5 ± 0.3	17.0 ± 0.7
^{82}Sr	3150	lead[c]	5.2 ± 0.2	11.2 ± 0.5

[a]Coincident response of a pair of 8 mm x 30 mm x 50 mm deep NaI(Tl) crystals to 1.2 mm diam sources

[b]to stop all positrons

[c]to suppress positron range effects

tron range effects were noticeable for ^{68}Ge and ^{82}Sr (due to their high positron energy).[29-30] The range effects were demonstrated by repeating the measurements with the ^{82}Sr source encased in lead. The results for ^{22}Na show that when the positron energy is low, range effects are not noticeable when using 8 mm wide crystals. The coincidence rate dropped by a factor of 6 when a cylinder of water (20 cm diameter and 20 cm high) was introduced but the resolution was not measureably degraded because the angular distribution of the scattered coincident events is quite broad.

The crystal pair resolution shown in Table I is a combination of three factors:

1) the geometrical resolution (one half the crystal width or 4 mm FWHM in our case),
2) the angular uncertainty of approximately 0.8 mr FWHM that arises because the positron-electron system does not annihilate at rest[31-32] (this contributes 1.6 mm FWHM in our case),[33] and
3) the range of the positrons in tissue.

When positron range effects are small (such as for ^{82}Sr in lead), the combination of geometrical resolution and angular uncertainty is 5 mm FWHM, in agreement with the above considerations. The resolution in the reconstructed transverse section is somewhat poorer than the crystal pair resolution (see below, section 3.8).

2.3 Lightpipe Transmission

The quartz lightpipes have very good optical transmission for NaI(Tl) scintillation light; most of the light lost is that which is not captured by total internal reflection. The transmission of the three lightpipes (relative to a direct crystal-PMT coupling) is 70%, for the 0° lightpipe and about 40% for the 60° and 90° lightpipes.

The coded lightpipe scheme discussed in Ref. 17 was not used due to the lower light transmission (≈20%), the resulting loss in time resolution, and the reduced control over the output of each crystal.

2.4 Phototubes

Two low-cost 38 mm phototubes were investigated in detail, the RCA 6199 and the newer RCA 4855. The gain of both types was adequate to provide a 511 keV photopeak anode signal of -1 V into a 1000 ohm load.

In table II we compare the relevant properties of these phototubes and conclude that the RCA 4855 is best for this application.

We are having rectangular phototubes 10 mm x 35 mm fabricated to demonstrate the possibility of eliminating the light pipes and to permit the design of a multiple ring system for the simultaneous imaging of several sections.

2.5 Pulse Height and Time Resolution

When coupled directly to a bialkali phototube the NaI(Tl) crystals have an energy resolution of 8 to 11% FWHM at 511 keV and a crystal pair time resolution of 4-6 ns FWHM. When these crystals were coupled to RCA 4855 phototubes via the lightpipes shown in Figs. 1,2, the energy resolution was 10 to 13% FWHM at 511 keV and the crystal pair time resolution was 5 to 7 ns FWHM.

The 511 keV photopeak pulse height resolution of the two groups of 8 crystals was 17% FWHM, larger than the individual crystal resolution because of phototube gain drift (typical 5% day-to-day variations) and the fact that the phototube voltages were only adjustable in 20 volt steps (corresponding to gain changes of 12%). The overall time jitter for the two groups of 8 had a FWHM of 15 nsec and 81% of the true coincidences fell within a 20 nsec coincidence window.

Table II - Phototube Properties

Tube Type	RCA 6199	RCA 4855
Photocathode	S-11	Bialkali
Photocathode radiant sensitivity (microamperes per blue lumen)[a]	3-10	10-13.5
No. of tubes tested	12	6
Dark pulse rate[b]	500 to 10,000 sec^{-1}	50 to 200 sec^{-1}
Time resolution (FWHM)[b,c]	5-12 nsec	5-7 nsec
Energy resolution[c] (FWHM at 511 keV)	10-17%	9-12%
Pulse height variation 300 to 30,000 cps 511 keV	5% max	4% max

[a] measurements supplied by RCA for a large number of each type.

[b] 15 keV threshold

[c] using crystal-lightpipe-phototube assembly as per Fig. 1.

2.6 Electronics

The electronics were designed for the full 280 crystal ring (fig 3) but only the portion needed to run two groups of 8 crystals was used for the studies reported in this paper. A timing signal was derived from the leading edge of the anode pulse by a threshold discriminator located at the base of each phototube. The anode pulses were -1V for the 511 keV photopeak and the threshold discriminators were set at -30mV which corresponds to about 15 keV. The timing signal was subsequently reduced in width to 20 ns and ORed with the corresponding pulses from the other 7 crystals of the group. The resulting signals from the two groups were then sent to a coincidence gate which required a 10 ns overlap. The effective coincidence resolving time was 20 ns. The timing differences among the various phototube channels were compensated by adjusting RC integrators located between the threshold discriminators and the 1.5 μs one-shots.

In the full system the timing signals from the 280 bases will be ORed together in groups of 8 to generate a timing signal for each of the 35 groups. Each group will then be put in coincidence with the opposing 14 groups (112 crystals) to provide the 50 cm field of view needed for clinical studies. Thus only 35 coincidence gates are used for 245 group pair combinations (15,680 crystal pair combinations). For the studies reported in this paper a 30 cm field of view was sufficient and only 8960 line integrals were measured.

Every time a coincidence is detected between two groups the following takes place:

(1) additional circuits determine the addresses of the crystals involved and provide reset pulses if this includes more than one crystal on each side. A switch selectable option provides additional sensitivity by permitting adjacent crystal pair detections to be used.

(2) The analog signal from the last dynode of each tube is gated to one of two analog-to-digital converters. For the 16 crystal system, the digitized pulse height was electronically compared to a pulse height window defined by manual switches. For the full 280 crystal system a digital pulse height window will be set automatically for each tube by a calibration sequence controlled by a microprocessor.

2.7 Crystal Cross-Talk

The electronics were set to veto any event where either coincident gamma ray interacted in more than one crystal. To measure this effect a well-collimated beam of 511 keV gamma rays ≃ 1 cm wide was directed toward the center of a group of 8 crystals. With threshold discriminators set at 50 keV, single, double and triple crystal interactions occurred with a probability of 84%, 15% and 1.0% respectively. In this test the multiple interaction veto rejected 16% of the single gamma detections and 30% of the coincident events. Of these multiple interactions, 62±3% involved adjacent crystals and 22±1%, 9±1% and 6±1% involved pairs of crystals separated by 1, 2 and 3 crystals respectively.

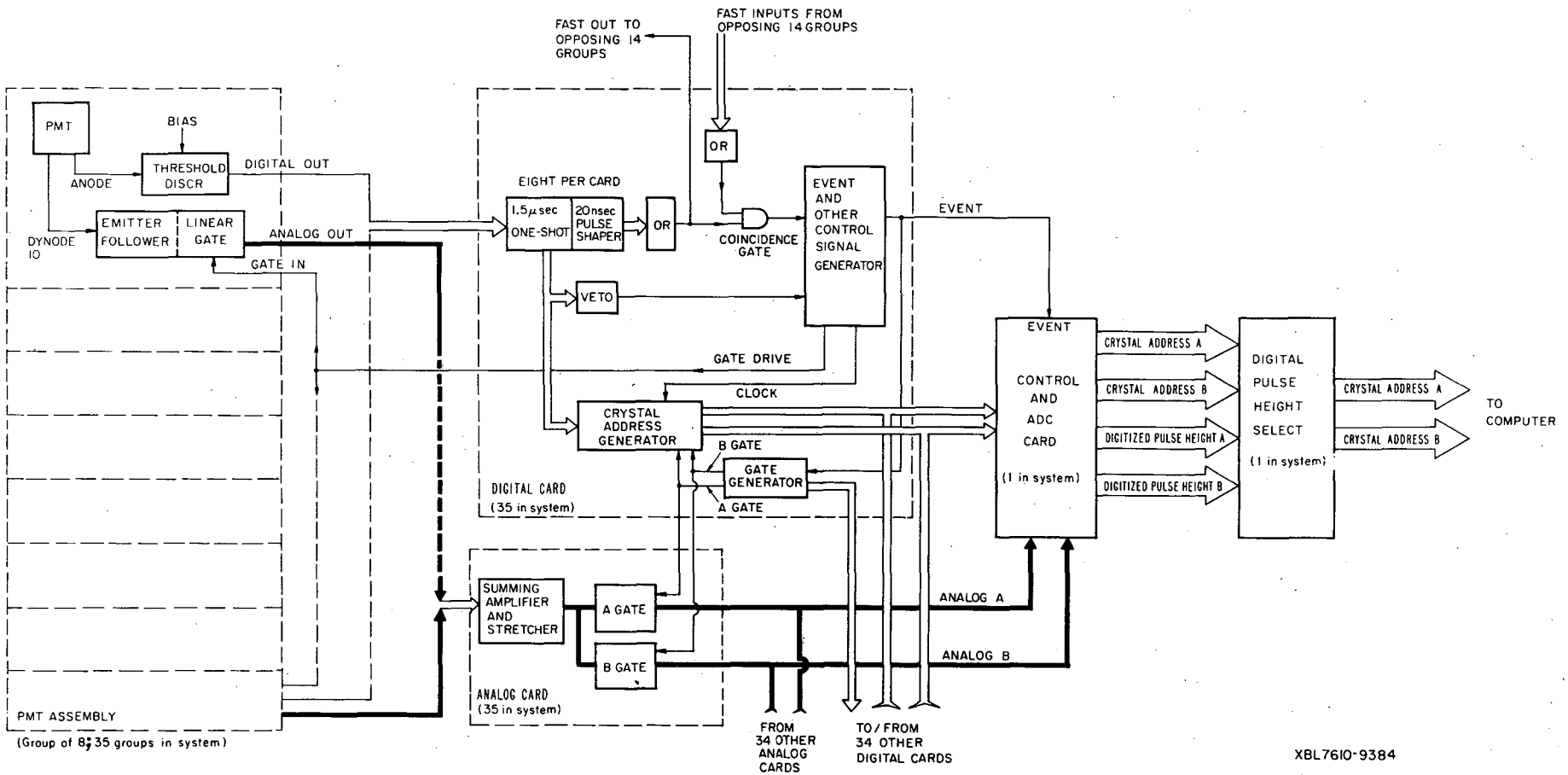

FIG 3: Block diagram of the electronics for the 280 crystal system. See section 2.6 of text for details.

3. Imaging Procedure and Results

3.1 Data Collection

To physically simulate the 280 crystal system we set up two opposing groups of eight crystals and rotated various test sources (phantoms) on a turntable between them (fig 4). A pair of lead blocks 20 cm x 20 cm x 5 cm was placed in front of each crystal group to form an adjustable shielding slit 20 cm deep and typically 1 to 2 cm wide. This shielding determined the thickness of the section to be imaged and blocked radiation emitted by activity external to that section. One group of 8 crystals was moved to 4 positions and at each position the turntable was automatically rotated to 35 evenly spaced angular positions. At each of these 4 x 35 = 140 views, 64 combinations of the coincident crystal pairs were recorded on magnetic tape by an on-line minicomputer. The resulting 8960 crystal pair combinations uniformly spanned a 30 cm diam circular region. These data were organized into 140 views (1.29^{o} angular sampling) of 64 parallel rays (4.9 mm spatial sampling)[3,4] The set-up used four RCA 4855's and 12 RCA 6199's.

It was necessary to correct the projection data for variations in sensitivity among the 8 x 8 = 64 crystal pairs. These variations were typically 10% and ranged as high as 30%, due mostly to variations in the size and time resolution of the assorted prototype crystals used. Prior to every phantom run, the relative sensitivities were determined by recording about 2 million events from a stationary uniform ^{68}Ga line source placed between the two crystal groups.

3.2 Reconstruction of Images from Projection Data

All the images presented in this paper were reconstructed by first correcting the projection data by attenuation factors calculated from the known geometry, then filtering the projections with the filter suggested by Shepp and Logan[9] and finally backprojecting those filtered projections into a circular array 128 pixels in diameter (2.45 mm/pixel). (When a coarser 64 pixel array with 4.9 mm/pixel was used the image resolution was seriously degraded). The reconstructions were performed on a CDC7600 and each required 12 sec of central processing time.

3.3 Coincidence Rates and Background Fractions for a Line Source on the Ring Axis

The coincidence rates and background fractions were measured using the set-up of fig. 4 and a line source of ^{68}Ge (1.2 mm diam, 90 mm long) positioned on the ring axis. Three categories of time coincident events are:

1) "true" events: unscattered (i.e. collinear) annihilation pairs originating from the same positron and detected in true time coincidence within the pulse height window.

2) "scattered" events: annihilation pairs originating from the same positron but one or both have scattered before being detected in true time coincidence and both are within the pulse height window.

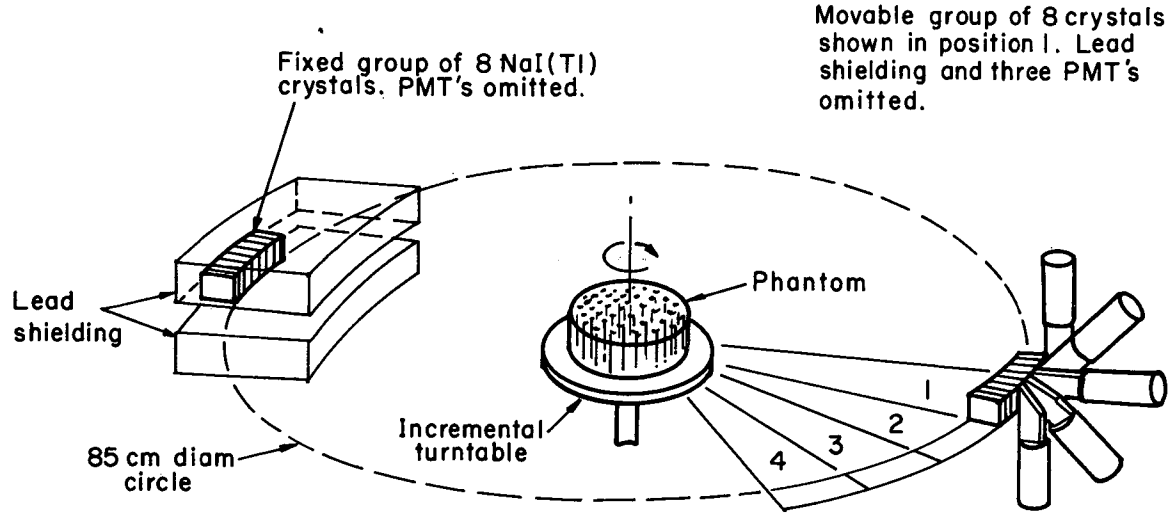

XBL7610-9349

FIG 4: Imaging set-up consisting of two opposing groups of eight rectangular NaI(Tl) crystals. Central turntable was automatically rotated to 35 evenly spaced angles for each of four positions of the moveable group to measure coincident events along 8960 projection integrals as they will be measured by the full 280 crystal ring.

3) "accidental" events: two gamma rays originating from different positrons but detected in accidental time coincidence (i.e. within 20 ns) and within the pulse height window. Such gamma rays can either be scattered or unscattered.

Note that only true events provide useful spatial information, while the scattered and accidental events produce a broad, heterogeneous background on the true image. Thus for a line source parallel to the ring axis we could readily separate true from background events because the former contribute only to chords that pass through or near the source. The accidental and scattered events contribute to the vast majority of chords that do not pass near the source. The accidental events were separately measured after delaying the fast timing signal from one group of 8 crystals by 100 ns. In this way we measured the coincidence rates and background fractions for a line source in air and in 20 cm water; for shielding gaps of 1, 1.5, and 2 cm; and several pulse height windows. Results are shown in Table III. In the absence of a scattering medium the true event rate was high and the background fractions were low. When the line source was centered in a cylinder of water 20 cm diameter and 20 cm high, the true event rate was reduced by a factor of 6, but the scattered and accidental rates were not greatly affected. As the shielding gap S was reduced from 2 cm to 1.5 and 1 cm, the true event rate varied as S^2, the scattered event rate varied as S^3, and the accidental event rate varied as S^4 as described in Ref. 17.

Photopeak selection reduced the true event rate by a factor of 6 and the scattered event rate by a factor of 10 for the line source in 20 cm of water and a 2 cm shielding gap. This suggests that most of the scatter background consists of small angle scatter and is not strongly reduced by a 450 keV pulse height threshold. The accidental event rate was reduced by a factor of 33, but this is higher than the accidental rate that would result by simply reducing the activity sixfold and using the 100-650 keV selection.

We also used a double pulse height window from 100-340 and 450-650 keV to exlude pulses in the 340-450 keV band between the 511 keV Comton edge and the photopeak, but there was no significant reduction in the background fraction. The successful use of this approach apparently requires better pulse height resolution and a tighter photopeak window.

3.4 Effect of Scatter Filters

The potential benefits of lead and indium scatter filters were investigated for a line source on the ring axis in a cylinder of water 20 cm in diameter and 20 cm high. The scatter filters were placed in front of both shielding gaps. The results (Table IV) show that scatter filters of various thicknesses reduce the true and scattered events by almost the same fraction. These data corroborate the limited effect of photopeak selection in reducing the scattered events and provide additional evidence that the scattered coincident events result from forward scattered gamma rays that are nearly as penetrating as the unscattered 511 keV annihilation radiation. On the other hand, the accidental fraction is noticeably reduced for lead sheets $\approx$ 0.5 mm thick but not much more for thicker sheets (1 to 3 mm), because the single counts that create the accidental events have a broad energy spectrum and the lead is predominantly effective in filtering out only the lower energy components.

Under the assumption that scatter filters would be used primarily to reduce the accidental background and permit higher imaging rates, we calculated the background that would result if the activity were adjusted for each scatter filter to provide a fixed true coincident rate. The result (Table V) shows a broad minimum in the background fraction around 0.6 mm of lead and larger backgrounds for the thicker layers used by Muehllehner.[19]

We conclude that scatter filters have only marginal utility for the type of instrument discussed in this paper and should be used only when high rates are required and some loss in sensitivity can be tolerated.

3.5 Distributed Sources

When the positron activity is distributed throughout the scattering medium, the attenuation is lower than for a source at the center.

The transmission F(r,R) for a point positron source at a distance r from the center of an absorbing cylinder of radius R is given by

$$F(r,R) = \frac{1}{2\pi} \int_0^{2\pi} \mathrm{EXP}\left(-2\mu \sqrt{R^2 - r^2 \sin^2\theta}\right) d\theta \quad (1)$$

where μ is the linear attenuation coefficient at 511 keV, and θ is the flight direction of the annihilation photons. For a positron source uniformly distributed over the entire cylinder, the transmission factor $f_D(R)$ is given by

$$f_D(R) = \frac{\int_0^R F(r,R)\, r\, dr}{\int_0^R r\, dr} \quad (2)$$

and for a source at the center the transmission factor $f_C(R)$ is given by

$$f_C(R) = \mathrm{EXP}(-2\mu R) \quad (3)$$

These attenuation factors are given in Table VI for various cylinders of water. Thus the sensitivity of the 280 crystal ring for an attenuated source is the sensitivity in air [140 counts per sec per (μCi/cm) for S = 2 cm] multiplied by the appropriate transmission factor from Table VI.

Table III - Effect of Scattering Material, Pulse Height Selection and Shielding Gap on the Coincidence Rate and Backgrounds[a]

Scattering Material (cm water)	Pulse Height Window (keV)	Shielding Gap S (cm)	Singles per Crystal (sec^{-1})[c]	Total Coincidences (sec^{-1})	True Events (sec^{-1})	Scatter Background (sec^{-1})	Accidental Background (sec^{-1})	Total Background (sec^{-1})
1.5[b]	100-650	2	3720	26,640	23,600(0.89)[d]	1360(0.05)	1630(0.06)	3040(0.11)
1.5	100-650	1	1140	6,295	5,960(0.95)	155(0.025)	180(0.030)	335(0.055)
20	100-650	2	3410	6,560	4,000(0.61)	1160(0.18)	1400(0.21)	2560(0.39)
20	100-650	1.5	1920	3,540	2,480(0.70)	525(0.15)	535(0.15)	1060(0.30)
20	100-650	1	1000	1,363	1,095(0.80)	140(0.10)	128(0.09)	268(0.20)
20	450-650	2	3410	837	680(0.81)	115(0.14)	42(0.05)	157(0.19)
20	100-340 and 450-650	2	3410	5,465	3,390(0.62)	960(0.18)	1115(0.20)	2075(0.38)

[a]Line source with 200 μCi/cm was aligned with the ring axis and extended 4 cm above and below section being imaged. Source was centered in scattering material. Coincidence resolving time was 20 ns. All coincident rates were summed over 140 views of the 16 crystal system and apply directly to the 280 crystal system.

[b]Source was 1.2 mm diam in a 13 mm lucite cylinder to stop all positrons

[c]Counts above dark counts (100 keV threshold)

[d]Fraction of total

Table IV - Effect of Scatter Filters on Coincidence Rate and Backgrounds[a]

Filter Thickness Pb (mm)	Singles per crystal[b] (sec^{-1})	Total Coincidences (sec^{-1})	True Events (sec^{-1})	Scatter Background (sec^{-1})	Accidental Background (sec^{-1})	Total Background (sec^{-1})
0	3410	6560	4000(0.61)[c]	1160(0.18)	1400(0.21)	2560(0.39)
0.15	2990	5940	3800(0.64)	1060(0.18)	1080(0.18)	2140(0.36)
0.31	2690	5390	3600(0.67)	930(0.17)	860(0.16)	1790(0.33)
0.64	2480	4770	3300(0.69)	830(0.17)	640(0.13)	1470(0.30)
1.35	2020	3780	2670(0.71)	620(0.16)	490(0.13)	1110(0.29)
1.35[d]	1870	3400	2410(0.71)	560(0.16)	430(0.13)	990(0.29)
1.98	1780	3010	2170(0.72)	490(0.16)	350(0.12)	840(0.28)
2.97	1440	2110	1550(0.73)	330(0.16)	230(0.11)	560(0.27)

[a]Same conditions as Table III with S = 2 cm and a 100-650 keV pulse height window

[b]Counts above dark counts (100 keV threshold).

[c]Fraction of total

[d]1.35 mm Pb, 0.76 mm In, 0.25 mm Cu as used in Ref. 19.

Table V - Optimization of Scatter Filters[a]

Filter Thickness Pb (mm)	Activity per cm required for true event rate of 4000/sec	Scatter Background (sec^{-1})	Accidental Background (sec^{-1})	Total Background (sec^{-1})
0	200	1160(0.18)	1400(0.21)	2560(0.39)
0.15	211	1116(0.18)	1197(0.19)	2313(0.37)
0.31	222	1033(0.17)	1062(0.17)	2095(0.34)
0.64[b]	242	1006(0.17)	940(0.16)	1946(0.33)
1.35	300	929(0.15)	1100(0.18)	2029(0.34)
1.35[c]	332	929(0.15)	1185(0.20)	2114(0.35)
1.98	369	910(0.15)	1190(0.20)	2100(0.34)
2.97	516	851(0.13)	1531(0.24)	2382(0.37)

[a]Conditions same as Table IV but activity has been adjusted to provide 4000 true events sec^{-1}

[b]Thickness that minimzes the total background fraction assuming that the amount of activity is not a constraint

[c]1.35 mm Pb, 0.76 mm In, 0.25 mm Cu.

Table VI - Calculated Transmission Factors for Positron Sources within Water Absorbers

Diameter of Water Absorber (cm)	Transmission factor for distributed source (eqn 2)	Transmission factor for source at center (eqn 3)
0	1.000	1.000
5	0.668	0.619
10	0.450	0.384
15	0.306	0.238
20	0.210	0.147
25	0.145	0.0912
30	0.102	0.0565

3.6 Angular Distribution of Scattered Background Events

The angular distribution of scattered events was measured for both 100-650 keV and 450-650 keV pulse height windows for a line source on the ring axis at the center of a 20 cm diam cylinder of water. The results (Fig. 5) show two main features:

1) The 100-650 keV angular distribution is only slightly flatter than that given by the Klein-Nishina relationship for single Compton scattering on free electrons.

2) The 450-650 keV angular distribution falls sharply to zero at about 30°, as expected from the Compton angle-energy relationship for single scattering:

$$\cos\theta = 2 - \frac{511 \text{ keV}}{E}$$

where θ is the scattering angle and E is the energy of the scattered photon. We conclude from these results that in 20 cm of water single scattering predominates and may be used for estimating energy and angular distributions. These results explain why neither the 450-650 keV pulse height selection nor the scatter filters were able to substantially reduce the scatter background, since restricting the field of interest to 30 cm diam already imposed an approximate cut-off of 40° in angle and 415 keV in energy.

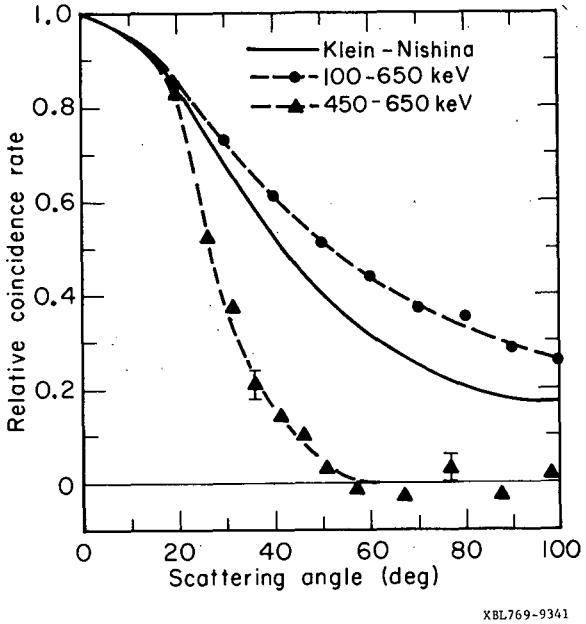

FIG 5: Angular distribution of scattered coincident events. Solid curve: Klein-Nishina angular distribution. Circles: Measured coincidences within a 100-650 keV pulse height window. Triangles: 450-650 keV pulse height window. Accidental coincidence background was subtracted.

3.7 The Effective Section Thickness for True and Background Events

As a measure of the ability of the lead shielding to block radiation originating from activity outside the section being imaged, we set a 9 cm long line source parallel to the plane of the ring in a cylinder of water 20 cm in diameter and 20 cm high and translated the source along the ring axis. The relative rate of true, scattered, and accidental events as well as single counts on one crystal are plotted in Fig. 6 as a function of source position for a 2 cm shielding gap. All rates are maximum on the central plane (source position zero) and fall off on either side of the plane. True events have the narrowest response with a FWHM of 1.2 cm while the scattered and accidental events have FWHM of 3.0 and 3.5 cm respectively. Integrating these curves to simulate a uniform sheet source along the ring axis we find that approximately 3 times as much activity contributes to the background events (both scatter and accidental) as contributes to the true events, as expected from analytical considerations.[17]

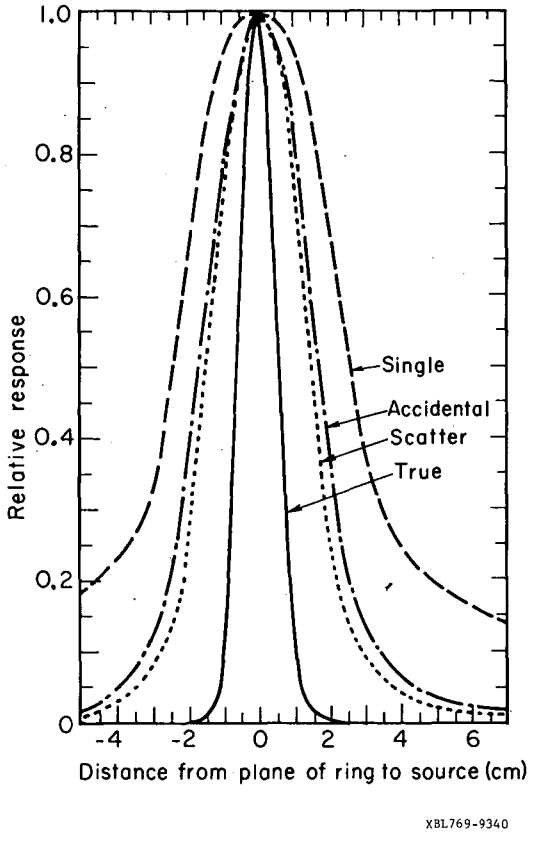

FIG 6: Relative response of the set-up of Fig. 4 to a source moving along the ring axis.

3.8 Measured Resolution in Transverse Section Images

The point source response in air was measured by imaging a 1.2 mm diam line source of ^{68}Ge set parallel to the ring axis at seven radii, from R=0 to R=15 cm in 2.5 cm steps. Fig. 7 is a superposition of the seven reconstructed images and shows that while the point spread function (PSF) is circular at R = 0, it elongates radially with increasing distance from the ring axis. The FWHM and FW(0.1)M of the radial and tangential profiles of the PSF are plotted in Fig. 8. Note that the tangential profile is nearly independent of radius while the radial profile grows rapidly beyond 10 cm. The reducion in the width of the tangential PSF with increasing R is the result of an artifact of the reconstruction algorithm that causes the PSF to drop more steeply below zero with increasing R.

The radial and tangential line spread functions (LSF) for R=0 and R=10 cm were determined by projecting the PSF onto the appropriate horizontal and vertical axis. (Fig. 9). The modulation transfer functions (MTF) were determined by numerically evaluating the cosine Fourier transforms of the corresponding LSF and represent the ability of the system to image various frequency components (Fig 10).

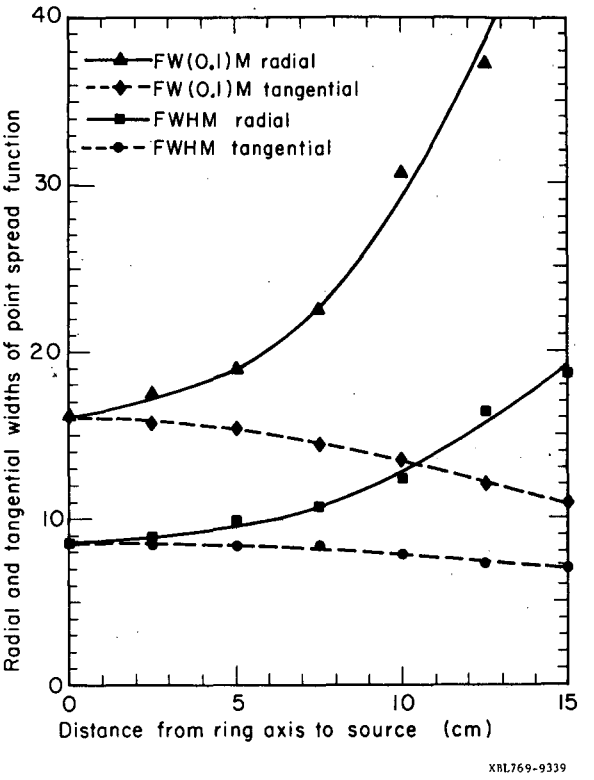

FIG 8: Widths of the radial and tangential profiles of the point spread functions shown in Fig. 7.

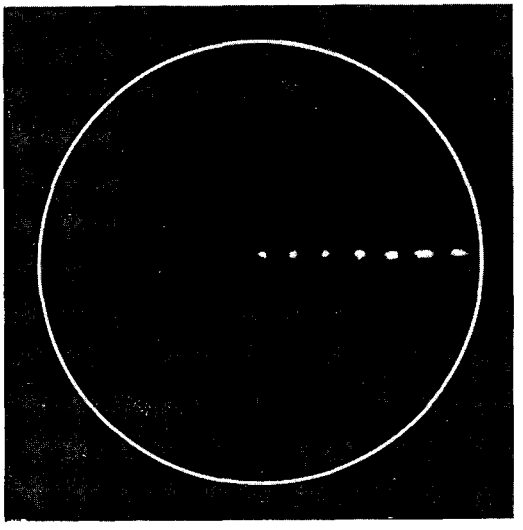

POINT SOURCE RESPONSE IN AIR

R=0, 2.5, 5, 7.5, 10, 12.5, 15 cm

FIG 7: Superposition of seven images of a line source 1.2 mm in diameter set parallel to the ring axis at various radii (R). Note the radial elongation for points distant from the ring axis.

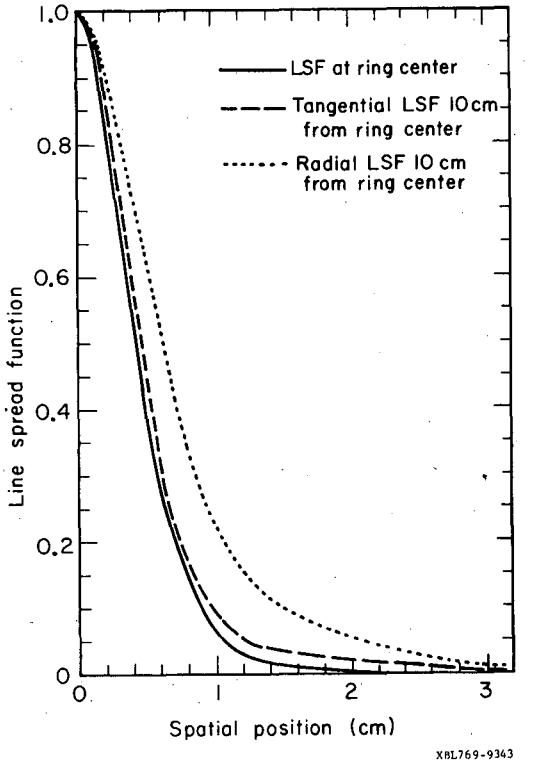

FIG 9: Line spread functions determined by projecting the R=0 and R=10 cm point spread functions of Fig. 7 onto horizontal and vertical axes.

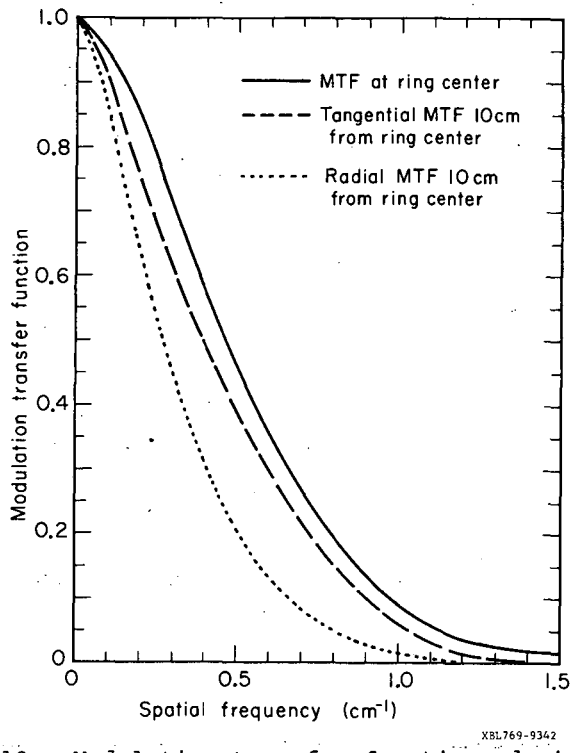

FIG 10: Modulation transfer functions derived from the line spread functions of fig 9.

Note that the resolution in transverse section is poorer than the crystal pair resolution of 6 mm FWHM described in section 2.2 because of the limited spatial sampling of 0.5 cm. With this spatial sampling frequency of 2 cm^{-1} the sampling theorm states that the highest spatial frequency that we can expect to observe is 1 cm^{-1}. The MTFs shown in Fig. 10 are in agreement with this prediction. At R=0 the LSF has a FWHM of 7.5 mm. For R > 0 the radial LSF is further degraded by the increase in the apparent size of the crystals when viewed by chords distant from the ring axis. At R=10 cm the radial and tangential LSFs have FWHM of 12.5 mm and 9.5 mm, respectively. For points at increasing radii there is an increase in the average solid angle seen by the crystals. The relative coincidence rates at R=0, 5, and 12.5 cm were 1.00, 1.04, and 1.08 respectively.

We have found, as expected, that the presence of 20 cm of water absorber does not effect our measured resolutions because the scattered and accidental events constitute a very broad background and the geometry and attenuation coefficients are well known. For the LSF in 20 cm Lucite, see ref 28 fig. 2.

3.9 Phantom Imaging in Transverse Section

To evaluate the ability of the system to image distributed sources containing hot and cold spots of several sizes and spacings we constructed two phantoms:

(1) a hot spot phantom consisting of a solid Lucite cylinder 20 cm in diam and 7.5 cm thick with triangular arrays of holes of diameters 2.5, 3, 3.5, 4, 5, and 6.25 mm and center-to-center spacings 10, 12, 14, 16, 20, and 25 mm, respectively.

(2) a cold spot phantom consisting of a hollow Lucite cylinder 15 cm in diam and 4 cm thick with Lucite poles of diameters 6 and 9 mm and center-to-center spacings of 19 and 23 mm respectively.

The patterns were adapted from the Anger pie phantom used to measure the resolution of Anger gamma cameras [35]. The voids in the phantoms were filled with a solution of 70% glycerol and 30% water to provide a uniform linear attenuation of 0.115 cm^{-1} (at 511 keV) through both the isotope solution and the Lucite. [When the cold spot phantom was filled with water (attenuation coefficient 0.096 cm^{-1}) the greater attenuation along rows of Lucite poles greatly enhanced the appearance of the poles as cold spots so that even the 6 mm cold spots were easily visible with 10^6 events.] The phantoms were injected with ^{68}Ga-EDTA to the desired activity level and re-injected every 20 to 40 min to keep the activity level within 20% of the initial value. The volume of water thus introduced was small and did not appreciably change the attenuation. To correct for source decay and re-injection, the time spent per view was controlled by a separate NaI(Tl) counter that constantly monitored the activity in the phantom.

For the studies described below, the shielding gap S was 2 cm, the pulse height window was 100-650 keV and the coincidence resolving time was 20 ns.

Fig. 11 shows images of the hot spot phantom for 0.5 and 1.5 million detected events. The activity density was 200 μCi/cm and the imaging time to collect 1.5 million events was 270 sec per view for 140 views or 10.5 hours total. The same data could be collected by the 280 crystal system in 270 sec. Of all the coincident events recorded, about 17% were scatter events and 21% were accidental events. Note that this background applies to a 30 cm field of view and only about 50% falls into the 20 cm phantom image. The peak-to-valley ratio for the hot spots with 25, 16 and 12 mm pitch was 8,3, and 1.5, respectively. The 12 mm pitch hot spots are not well seen in the 0.5 million event image because of statistical fluctuations and the small peak-to-valley ratio, but they appear more clearly on the 1.5 million event image. This indicates that with even more events, the 10 mm pitch hot spots could be just resolved, in accord with the MTF (Fig. 10).

Fig. 12 shows an image of the cold spot phantom for 1 million detected events. The activity density was 300 μCi/cm and the imaging time was 70 sec per view for 140 views or 2.7 hours total. The same data could be collected by the 280 crystal system in 60 sec.

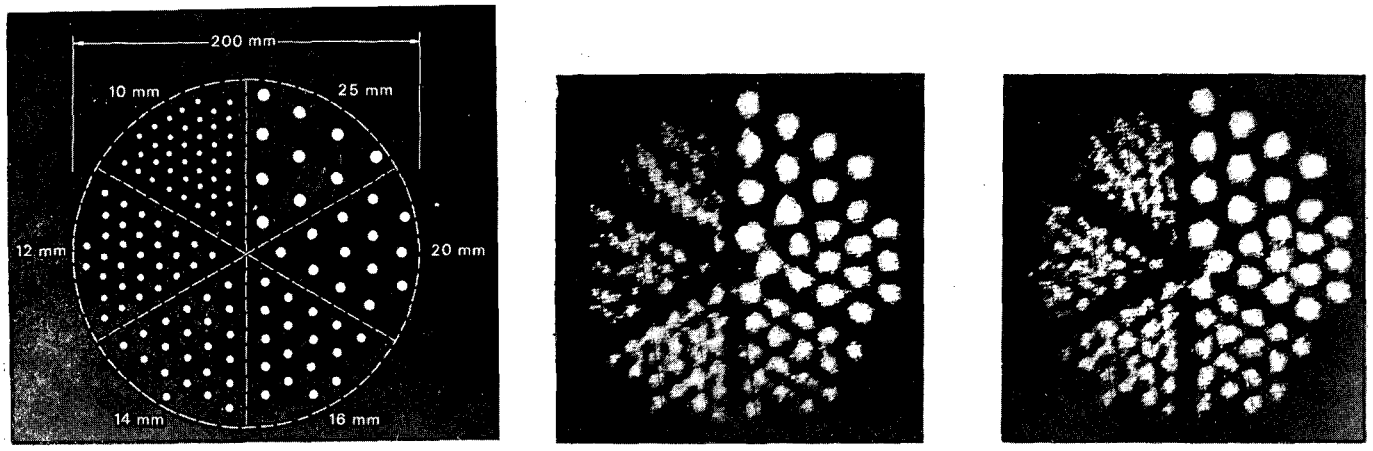

FIG 11: Images of the hot spot phantom using ^{68}Ga and the set-up of Fig. 4. See section 3.9 of text for details.

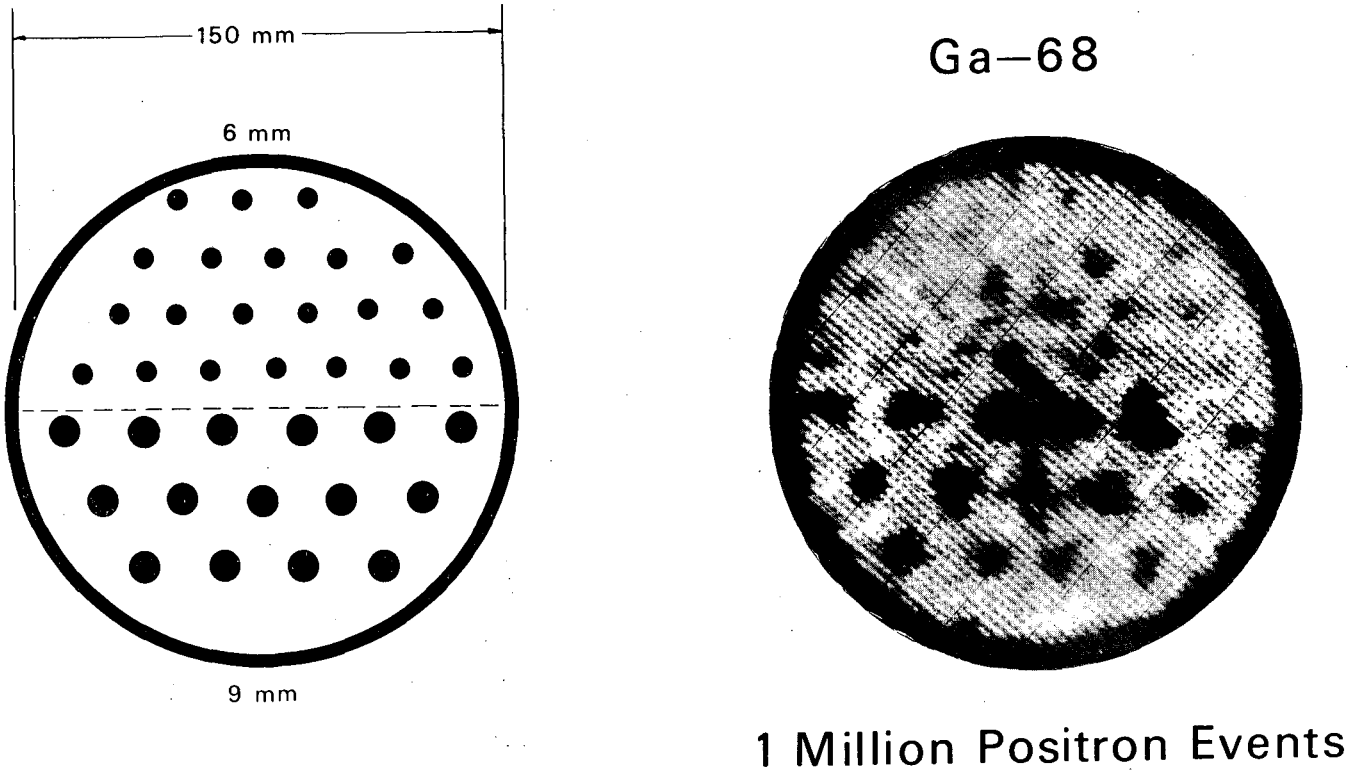

FIG 12: Images of the cold spot phantom using ^{68}Ga and the set-up of Fig. 4. See section 3.9 of text for details.

Of all the coincident events recorded, about 16% were scattered events and 16% were accidental events. Note that only about 35% of this background falls into the 15 cm phantom image. The plateau-to-hole ratio for the cold spots 9 mm in diam was 2.0. All 15 of the 9 mm cold spots are clearly seen but the 6 mm cold spots have less image contrast and are obscured by statistical fluctuations.

3.10 Statistical Requirements

We have previously analyzed the statistical requirements of transverse section tomography for both positron coincidence detection using a ring of crystals and single photon detection using multiple view data from a gamma camera.[28,36-37]. In summary, the rms statistical noise is larger than that which would be expected from the statistics of the average number of detected events per resolution cell by a factor of $1.6\times(\text{number of resolution cells})^{\frac{1}{4}}$. This factor is about 8 for a uniform disc of positron activity 20 cm (30 resolution cells) in diameter and includes a 30% increase due to attenuation compensation. In this example 10^6 events yields a reconstructed image having 1400 events per cell with an rms uncertainty of 21%. When a smaller number of events must be used, such as in the dynamic imaging of blood flow, the reconstruction can be modified to provide activity measurements with useful statistical accuracy in larger but well-defined regions. For example, the 280 crystal ring will have the speed to collect 2×10^4 events in 2 sec if sufficient activity is present. The statistical uncertainty per 4 cm cell for a 6 x 6 cell array is 17%.

4. Conclusions

The distribution of positron-emitting isotopes can be imaged in 20 cm of water absorber with 7.5 mm FWHM resolution at an event rate of 10,000 events per sec by using a ring of 280 NaI(Tl) crystals, phototubes, and appropriate readout electronics. The background from scattered and accidental coincidences does not severely effect the ability to reliably detect 3.5 mm hot spots with a 14 mm center-to-center spacing and isolated 9 mm cold spots. These backgrounds are not substantially reduced by either photopeak selection or lead scatter filters. With an activity of 400 μCi per 1 cm thick section, two million events will be collected by the 280 crystal ring in about 3 min. The speed of this system is adequate for dynamic studies of brain and kidney blood flow and metabolism with 20% rms uncertainty in 4 x 4 cm regions if an event rate of 10,00 sec^{-1} is available from injected radiopharmaceuticals.

ACKNOWLEDGEMENTS

We are indebted to T. Shimizu and T. Vuletich for considerable technical assistance; to W. Greenberg for aid in data analysis and image reconstruction; and to Y. Yano and G. Roth for providing ^{68}Ga isotope. We thank H.O. Anger and F. Goulding for helpful discussions. This work was supported by NCI grant No. R01 CA-17566-01, NCI contract No. NIH Y01-CB-50304 and by the Energy Research and Development Administration.

REFERENCES

1. Rankowitz S., Robertson J.S., Higinbotham W.A. et al., Positron Scanner for Locating Brain Tumors, IRE Int Conv Record 10(9), 49-56, 1962.

2. Kuhl D.E., Edwards R.Q., Image Separation Radioisotope Scanning, Radiology 80, 653, 1963.

3. Kuhl D.E. and Edwards R.Q., The Mark III Scanner: A compact Device for Multiple-View and Section Scanning of the Brain, Radiology 96, 563-570, 1970.

4. Kuhl D.E., Edwards R.Q., Ricci A.R., and Reivich M., Quantitative Section Scanning using Orthogonal Tangent Correction, J Nucl Med 14, 196-200, 1973.

5. Keyes J.W., Jr., Kay D.B., Simon W., Digital Reconstruction of Three-Dimensional Radionuclide Images, J Nucl Med 14, 628, 1973.

6. Robertson J.S., Marr R.B., Rosenblum M.et al, 32 Crystal Positron Transverse Section Detector. In Tomographic Imaging in Nuclear Medicine, (Freedman G.S. ed) New York, Society of Nuclear Medicine, 1973, pp. 142-153.

7. Chesler D.A., Positron Tomography and Three Dimensional Reconstruction Techniques, Tomographic Imaging in Nuclear Medicine (Freedman G.S., ed), Society of Nuclear Medicine, New York (1973) 176.

8. Budinger T.F., Gullberg G.T., Three-Dimensional Reconstruction in Nuclear Medicine Emission Imaging, IEEE Trans Nucl Sci NS-21/3, 2-20, 1974.

9. Shepp L.A., Logan B.F., The Fourier Reconstruction of a Head Section, IEEE Trans Nucl Sci NS-21/3, 21-43, 1974.

10. Oppenheim, B.E., More Accurate Algorithms for Iterative 3-Dimensional Reconstruction, IEEE Trans Nucl Sci NS-21/3, 72-77, 1974.

11. Brownell G.L., Burnham C.A., Chesler D.A., et al., Transverse Section Imaging of Radionuclide Distributions in Heart, Lung, and Brain. In Workshop on Reconstruction Tomography, Ter-Pogossian M.M. et al., eds. Baltimore, University Park Press: to be published.

12. Budinger T.F., Gullberg G.T., Transverse Section Reconstruction of Gamma-ray Emitting Radionuclides in Patients. In Workshop on Reconstruction Tomography, Ter-Pogossian M.M. et al., eds., Baltimore, University Park Press: to be published.

13. Cho, Z.H., Eriksson L., and Chan J., A Circular Ring Transverse Axial Positron Camera, In Workshop on Reconstruction Tomography, Ter-Pogossian M.M. et al., eds., Baltimore, University Park Press: to be published.

14. Ter-Pogossian M.M., Phelps M.E., Hoffman E.J. et al., A Positron-Emission Transaxial Tomograph for Nuclear Imaging (PETT). Radiology 114, 89-98, 1975.

15. Phelps M.E., Hoffman E.J., Mullani N.A., et al., Application of Annihilation Coincidence Detection to Transaxial Reconstruction Tomography. J Nucl Med 16, 210-224, 1975.

16. Muehllehner G., Positron Camera with Extended Counting Rate Capability, J Nucl Med 16, 653-657, 1975.

17. Derenzo S.E., Zaklad H., and Budinger T. F., Analytical Study of a High-Resolution Positron Ring Detector System for Transaxial Reconstruction Tomography, J Nucl Med 16, 1166-1173, 1975.

18. Phelps M.E., Hoffman E.J., Mullani N.A., et al., Design Considerations for a Positron Emission Transaxial Tomograph (PETT III), IEEE Trans Nucl Sci NS 23/1, 516-522, 1976.

19. Muehllehner G., Buchin M.P., and Dudek J.H., Performance Parameters of a Positron Imaging Camera, IEEE Trans Nucl Sci NS23/1, 528-537, 1976.

20. Chang L.T., Macdonald B., and Perez-Mendez V., Axial Tomography and Three Dimensional Image Reconstruction, IEEE Trans NS23/1, 568-572, 1976.

Hattner R.S., Lim C.B., Swann S.J., et al., Cerebral Imaging Using ^{68}Ga DTPA and the U.C.S.F. Multiwire Proportional Chamber Positron Camera, IEEE Trans NS23/1, 523-527, 1976.

21. Cho Z.H., Chan J.K., and Eriksson L., Circular Ring Transverse Axial Positron Camera for 3-Dimensional Reconstruction of Radionuclides Distribution, IEEE Trans Nucl Sci NS23/1, 613-622, 1976.

22. Hoffman E.J., Phelps M.E., Mullani N.A., Higgins C.S., and Ter-Pogossian M.M., Design and Performance Characteristics of a Whole-Body Positron Transaxial Tomograph, J Nucl Med 17, 493-502, 1976.

23. Thompson C.J., Yamamoto Y.L., and Meyer E., Reconstruction and Analysis of Data from a Dynamic Positron Imaging Device. J Nucl Med 17, 543, 1976.

24. Budinger T.F., Gullberg G.T., Moyer B.R. et al., Transverse Section Imaging of the Myocardium, J Nucl Med 17, 552, 1976.

25. Correia J.A., Chesler D.A., Hoop B. Jr. et al., Transverse Section Reconstruction with Positron Emitters and the MGH Positron Camera, J Nucl Med 17, 551, 1976.

26. Jaszcczak R., Huard D., Murphy P., and Burdine J., Radionuclide Emission Computed Tomography with a Scintillation Camera, J Nucl Med 17, 551 (1976).

27. Keyes J.W., Orlandea N., Heetderks W.J., and Leonard P.F., The Humongotron-A Gamma Camera Transaxial Tomograph, J Nucl Med 17, 552 (1976).

28. Budinger T.F., Derenzo S.E., Gullberg G.T., Greenberg W.L. and Huesman R.H. "Emission Computed Axial Tomography", Lawrence Berkeley Laboratory Report LBL-4794, presented at IAEA Symposium on Medical Radionuclide Imaging, Los Angeles, California, October 25-29, 1976.

29. Phelps M.E., Hoffman E.J., Huang S.C. et al., Effect of Positron Range on Spatial Resolution, J Nucl Med 16, 649-652, 1975.

30. Cho Z.H., Chan J.K., Ericksson L., et al., Positron Ranges Obtained from Biomedically Important Positron-Emitting Radionuclides, J Nucl Med 16, 1174-1176, 1975.

31. Stewart A.T., Momentum Distribution of Metallic Elutions by Positron Annihilation, Canad J Phys 35, 168-183, 1957.

32. Colombino P., Fiscella B., and Trossi L., Study of Positronium in Water and Ice from 22 to - 144 ^{o}C by Annihilation Quantum Measurements, Nuovo Cimento 38, 707-723, 1965.

33. Muehllehner G., Resolution Limit of Positron Cameras, J Nucl Med 17, 757, 1976.

34. The sampling is actually on a 4.9 mm by 0.63^{o} grid but only every other grid point is sampled. The missing grid points could be sampled by rotating the ring one-half of a crystal spacing, but little additional information would be provided.

35. Anger H.O., Testing the Performance of Scintillation Cameras, Lawrence Berkeley Laboratory Report LBL-2027 (May 1973).

36. Friedman M.I., Beattie J.W., Laughlin J. S., Cross-sectional Absorption Density Reconstruction for Treatment Planning, Phys Med Biol 19, 819, 1974.

37. Huesman R.H., The Effects of a Finite Number of Projection Angles and Finite Lateral Sampling of Projections on the Propagation of Statistical Errors in Transverse Section Reconstruction, Lawrence Berkeley Laboratory Report LBL-4773, (July 1976).

This report was done with support from the United States Energy Research and Development Administration. Any conclusions or opinions expressed in this report represent solely those of the author(s) and not necessarily those of The Regents of the University of California, the Lawrence Berkeley Laboratory or the United States Energy Research and Development Administration.

TECHNICAL INFORMATION DIVISION
LAWRENCE BERKELEY LABORATORY
UNIVERSITY OF CALIFORNIA
BERKELEY, CALIFORNIA 94720